



Article

# Stepped-Tube Backside Cavity Piezoelectric Ultrasound Transducer Based on $\text{Sc}_{0.2}\text{Al}_{0.8}\text{N}$ Thin Films

Xiaobao Li <sup>1,2</sup>, Haochen Lyu <sup>2,3</sup>, Ahmad Safari <sup>3</sup> and Songsong Zhang <sup>1,2,\*</sup> <sup>1</sup> School of Microelectronics, Shanghai University, Shanghai 200444, China<sup>2</sup> Shanghai Melon Technology Company Ltd., Shanghai 201899, China<sup>3</sup> Department of Materials Science and Engineering, Rutgers, The State University of New Jersey, Piscataway, NJ 08854, USA

\* Correspondence: songsong.zhang@sitigroup.com

**Abstract:** This paper presents a novel piezoelectric micromachined ultrasonic transducer (PMUT) with theoretical simulation, fabrication, and testing. Conventional methods using a PCB or an external horn to adjust the PMUT acoustic field angle are limited by the need for transducer size. To address this limitation, the stepped-tube (expanded tube) backside cavity PMUT has been proposed. The stepped-tube PMUT and the tube PMUT devices have the same membrane structure, and the acoustic impedance matching of the PMUT is optimized by modifying the boundary conditions of the back cavity structure. The acoustic comparison experiments show that the average output sound pressure of the stepped-tube backside cavity PMUT has increased by 17%, the half-power-beam-width ( $\theta_{-3\text{dB}}$ ) has been reduced from  $55^\circ$  to  $30^\circ$  with a reduction of 45%, and the side lobe level signal is reduced from 147 mV to 66 mV. In addition, this work is fabricated on an eight-inch wafer. The process is compatible with standard complementary metal oxide semiconductor (CMOS), conditions are stable, and the cost is controllable, plus it facilitates the batch process. These conclusions suggest that the stepped-tube backside cavity PMUT will bring new, effective, and reliable solutions to ranging applications.

**Keywords:** PMUT; directivity; acoustic field; scandium-doped aluminum nitride ( $\text{Sc}_{0.2}\text{Al}_{0.8}\text{N}$ )



**Citation:** Li, X.; Lyu, H.; Safari, A.; Zhang, S. Stepped-Tube Backside Cavity Piezoelectric Ultrasound Transducer Based on  $\text{Sc}_{0.2}\text{Al}_{0.8}\text{N}$  Thin Films. *Micromachines* **2024**, *15*, 72. <https://doi.org/10.3390/mi15010072>

Academic Editors: Lin Zhang and Tian-Bing Xu

Received: 17 November 2023

Revised: 14 December 2023

Accepted: 27 December 2023

Published: 29 December 2023



**Copyright:** © 2023 by the authors. Licensee MDPI, Basel, Switzerland. This article is an open access article distributed under the terms and conditions of the Creative Commons Attribution (CC BY) license (<https://creativecommons.org/licenses/by/4.0/>).

## 1. Introduction

Piezoelectric Micromachined Ultrasonic Transducers (PMUTs) have gained significant attention in recent years. Conventional bulk piezoelectric transducers are gradually being replaced by Micromachined Ultrasonic Transducers (MUTs) due to their large size, incompatibility with CMOS processes, the requirement for acoustic matching layers, and other limitations [1]. Based on the sensing mechanism, MUTs can be categorized into two types: capacitive ultrasonic transducers and piezoelectric ultrasonic transducers. These transducers are thin-film in nature and have their acoustic impedance matched to the medium (acoustic or aqueous), eliminating the need for a matching layer. Compared to CMUT, PMUT does not require a bias current to operate, resulting in significantly improved device reliability. In the last decade, researchers have started conducting comprehensive research on PMUT. PMUT has been widely used in fingerprint identification, gesture recognition, medical imaging, flow meters, distance measurement, humidity sensors, and other applications [2–9].

Currently, various piezoelectric materials such as lead zirconate titanate (PZT), barium calcium zirconate titanate ceramics (BCZT), and aluminum nitride film (AlN) have been widely applied [8,10,11]. However, the preparation of PZT requires a high temperature environment ( $>480^\circ\text{C}$ ) due to the lead content in the process, which is gradually being replaced in today's environmentally conscious context. BCZT is a lead-free piezoelectric material, but its preparation also requires higher temperatures [11]. Compared to PZT and BCZT, the lead-free piezoelectric material AlN can be deposited at lower temperatures

(<300 °C), offering improved receiving sensitivity and temperature stability. It is characterized by a wide range of raw material sources and compatibility with CMOS processes [12]. Compared to pure AlN, the piezoelectric performance of ScAlN significantly improves while retaining many of the characteristics of AlN, such as being easy to deposit, etch, and being lead-free [13]. Therefore, in this paper,  $\text{Sc}_{0.2}\text{Al}_{0.8}\text{N}$  film-based PMUT is chosen for preparation.

In the process of ultrasonic propagation, there is attenuation and dissipation of sound wave energy. In order to enhance the detection distance and accuracy, a highly directional radiation mode is required. In addition to the main lobe, traditional PMUT also has side lobes during operation. The presence of side lobes can cause detection errors and other problems, such as incorrectly identifying other objects or echoes from the ground. Therefore, increasing the output sound pressure and improving the directivity of the sound field have been the focus of research for some time. Nayak et al. [14] received the radiation pattern of a single PMUT coupled with air by adjusting the PCB package size. Haolin Yang et al. [15], with an external horn, optimized the sound field angle of a 66 kHz PMUT array from  $100^\circ$  to  $20^\circ$  with a half-power-beam-width ( $\theta_{-3\text{dB}}$ ). Yuchao Zhang et al. [16] optimized the acoustic output of a single PMUT at a resonant frequency of 91 kHz with an external speaker. Scott et al. [17] at the University of California, Davis, optimized the device structure, MEMS process wafer, and CMOS process wafer level bonding to achieve an optimized back pressure recovery structure. This resulted in a 4.5 dB increase in sound pressure level and improved directionality. However, the side lobe level also increased accordingly. External PCB packaging and speakers will increase the size of the device, thereby negating the advantages of PMUT's small integration. By connecting an external speaker and adjusting the PCB package size, although the directivity of the PMUT improves and the sound pressure level increases, it does not significantly suppress the generation of side lobes.

In this paper, a new structure PMUT based on  $\text{Sc}_{0.2}\text{Al}_{0.8}\text{N}$  is theoretically analyzed, designed, simulated, prepared, and characterized. The height of the back cavity is controlled by stepwise etching. A stepped-tube backside cavity (expanded tube backside cavity) is introduced at the back of the PMUT. This cavity serves to inhibit the generation of side lobes while also enhancing the directivity of the acoustic field. The purpose of this is to focus the output energy more effectively, increase the acoustic pressure output, and regulate the angle of the sound field for the PMUT.

## 2. Design and Modeling

### 2.1. Theoretical Analysis

The structure of the new stepped-tube PMUT, as reported in this paper, is shown in Figure 1, and the membrane structure consists of an Mo/ $\text{Sc}_{0.2}\text{Al}_{0.8}\text{N}$ /Mo stack with thicknesses of 0.1  $\mu\text{m}$ /1  $\mu\text{m}$ /0.2  $\mu\text{m}$  on an SOI wafer, respectively. The difference lies in the structure of the backside cavity. The overall height of the two backside cavities in the PMUT is 500  $\mu\text{m}$ . The conventional structure is a tube backside cavity with a diameter of 750  $\mu\text{m}$ . The stepped-tube backside cavity is formed by two Deep Reactive Ion Etching (DRIE) to create an expanding tube resonance cavity at the bottom of the tube resonance cavity, with a height of 250  $\mu\text{m}$  and a diameter increment of 950  $\mu\text{m}$ .

According to an analysis of acoustic theory, the radiation impedance describes the process of matching the impedance of sound waves as they propagate from the diaphragm into the surrounding medium. When a sound source vibrates, it generates a sound field in the surrounding medium, and at the same time the source is also immersed in the radiated sound field in which it is situated. Therefore, it will also be subject to a certain reaction, which is equivalent to a force impedance being applied to the original mechanical vibration system. The real part is equivalent to mechanical damping, reflecting the existence of energy loss, vibration, and a sound source that will radiate sound energy [18]. The virtual component of the performance of the inertial force, which is equivalent to the sound source

itself on the mass of the additional radiation mass and vibration operates to overcome the inertial force and perform work, thereby storing energy in the system [19].

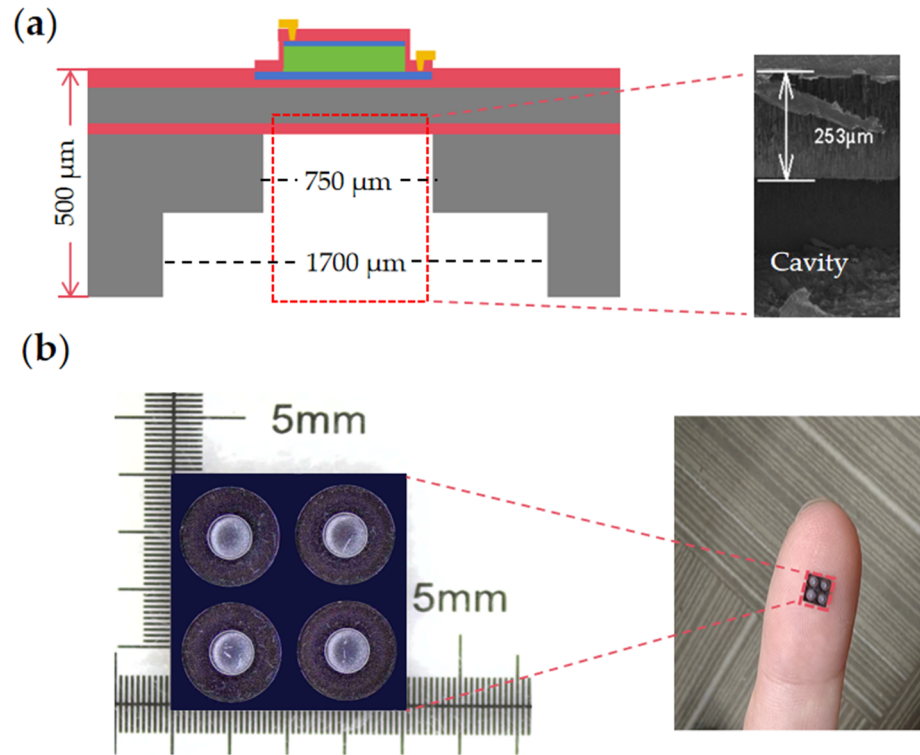


**Figure 1.** (a) Proposed PMUT, 2D structure schematic, and SEM backside cavity height localized view. (b) Optical microscopic top view of the backside cavity structure.

The horn consists of tubes with varying cross-sectional areas. Its advantage is that it can provide almost any acoustic impedance. The expression for the acoustic impedance of the horn throat is (1) [18]:

$$Z_{a0} = \frac{\rho_0 c_0}{S_0} \left[ \frac{Z_{a1} \cos(\gamma l + \theta) + j \frac{\rho_0 c_0}{S_1} \sin \gamma l}{\frac{\rho_0}{S_1} \cos(\gamma l - \theta) + j Z_a \sin \gamma l} \right] \quad (1)$$

where  $S_0$  is the opening area at the end of the horn,  $\rho_0$  is the density of the medium,  $c_0$  is the propagation speed of sound in the medium,  $l$  is the length of the horn,  $Z_{a1}$  is the acoustic impedance at the exit of the horn when  $ka$  is larger, the horn can be used as an approximation for the radiated acoustic impedance of the piston on the infinite baffle, and the change of the opening area of the horn can increase the radiated power while making the directionality of the sound source clearer and the energy more centralized [20]. The acoustic impedance of the PMUT,  $Z_{pmut}$ , and the radiated impedance,  $R_r$ , is calculated as in (2) and (3) [3].

$$Z_{pmut} = \frac{\rho_0 c_0}{A_m} \left( 1 - \frac{2J_1(2ka)}{2ka} + j \frac{2K_1(2ka)}{2ka} \right) \quad (2)$$

$$R_r = \left( \pi a_{eff}^2 \right)^2 R_1 \quad (3)$$

where  $J_1$  and  $K_1$  are the first-order Bessel and first-order Struve functions, and the radiation impedance is normalized as shown in Figure 2a [21], where the real part  $R_1$  is the radiation resistance, which determines the energy coupled to the medium by the PMUT, the imaginary part  $X_1$  is the radiation reactance,  $\rho_0$  is the density of the medium,  $c_0$  is the propagation speed of the acoustic wave in the medium,  $k$  is the number of waves,  $a$  and  $a_{eff}$  are the radius and the effective radius of the PMUT.  $A_m$  is determined by the radius

of the opening at the end of the backside cavity. The average radiated power  $\overline{W}_r$  can be obtained as (4) [20].

$$\overline{W}_r = \frac{1}{2} R_r u_a^2 \tag{4}$$

$$f = \frac{1.63}{r^2} \sqrt{\frac{D}{\sum \rho_i t_i}} \tag{5}$$

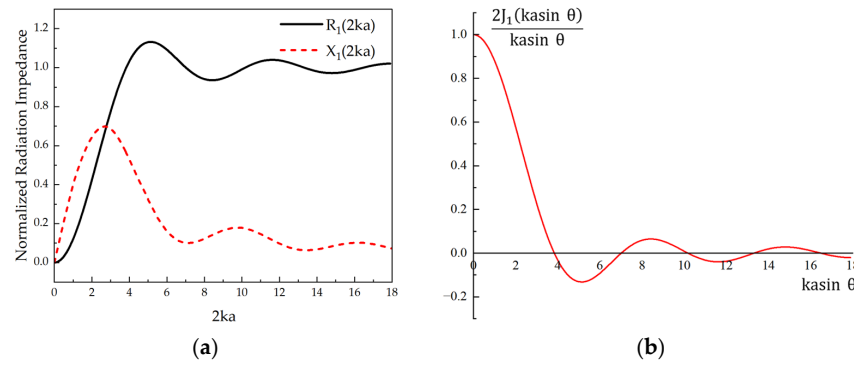


**Figure 2.** (a) Radiative impedance real part  $R_1(2ka)$  and imaginary part  $X_1(2ka)$  normalized to the characteristic impedance in air. (b) Normalized plot of the directivity function  $D(a, \theta)$ .

It can be observed that when the vibration speed of the sound source remains constant, the average radiated power value is influenced by the radiation impedance and the equivalent radiated area. The equivalent radiated area is determined by the number of waves and the effective radius of the device, which in turn depends on the radius of the opening at the end of the backside cavity. To increase the radiated power, it can be achieved by either increasing the effective radius of the device or increasing the frequency of the PMUT. From Equation (5), it can be seen that the frequency on the backside is usually inversely proportional to the square of the diaphragm radius [22]. The stepped tube on the backside cavity increases the equivalent radiant area of the PMUT while maintaining the frequency almost unchanged.

According to the Rayleigh principle, the sound pressure of PMUT at any point  $P(r, \theta)$  in the far field as in (6) [18]:

$$P(r, \theta) = j\omega \frac{\rho_0 u_a a^2}{2r} \left[ \frac{2J_1(kasin\theta)}{kasin\theta} \right] e^{j(\omega t - kr)} \tag{6}$$

$D(a, \theta)$  is a spatial distribution function that describes the radiated free far sound field. It characterizes the distribution of the acoustic field emitted by the transducer, the degree of concentration of the radiated power, the accuracy of the localization, and the discriminatory ability. Combined with  $P(r, \theta)$ , the normalized directivity function of the circular thin-film transducer is expressed as (7) [23]:

$$D(a, \theta) = \left| \frac{2J_1(kasin\theta)}{kasin\theta} \right| \tag{7}$$

As shown in Figure 2b, related to the directivity function are the wave number  $k$  and the equivalent radius  $a_{eff}$  of the PMUT. Since the environment in which the device operates is deterministic, the speed of sound in the medium  $c_0$  does not change. Therefore, what affects the directivity of a single-array transducer are the PMUT operating frequency and the equivalent radius  $a_{eff}$ .

From  $D(a, \theta)$ , it can be seen that as the operating frequency of the PMUT increases, the  $2ka$  increases and the directivity improves [18]. However, the corresponding side lobe also increases, and the sound pressure attenuation in the medium is inversely proportional to the transmission distance  $X$  as the frequency rises. Therefore, increasing the frequency

is not a good choice for improving the directivity of a single array element. Similarly, when the radius of the PMUT is larger, the directivity improves. However, the number of side lobes also increases gradually. Therefore, we aim to enhance the directivity of the single-array element by appropriately increasing its equivalent radius.

## 2.2. Modeling Analysis

In order to determine the structure of the backside cavity of the PMUT, the dynamic response of the PMUT is modeled using FEM (COMSOL 5.6) simulation software. The piezoelectric layer is made of  $\text{Sc}_{0.2}\text{Al}_{0.8}\text{N}$  film doped with 20% Sc and has a thickness of  $1\ \mu\text{m}$ . The main body of the elastic layer is made of top silicon and has a thickness of  $4\ \mu\text{m}$ . The height of the backside cavity is  $500\ \mu\text{m}$ . The average value of the acoustic pressure is measured at a location  $3\lambda$  underneath the backside cavity. The results are shown in Figure 3d [24]. When the height of the second layer backside cavity ( $H_c$ ) is small, the PMUT is considered to have a tube sound pressure gain by  $(500 - H_c)$  for the backside cavity height. Increasing the diameter of the second layer backside cavity does not result in sound pressure gain. This is because the reflected sound waves from the backside cavity wall and the PMUT output acoustic wave are reduced when they are superimposed, leading to a decrease in the output sound pressure [23]. From Figure 3a–c, when  $H_c$  is more significant, the backside cavity sound pressure gain directly benefits from the diameter increment of the second layer. This is because the effective area increases, resulting in an increase in radiated power when the diameter increment  $D_i = 950$ , the cavity height  $H_c = 400$ , and compared with the pipe PMUT, the average sound pressure at  $3\lambda$  below the stepped pipe backside cavity is improved by 120%. For a single PMUT, the larger backside cavity end opening obtains a larger effective radiating area, which can produce higher bulk velocity and higher sound pressure output, push more air, and convert other forms of energy into the acoustic energy of air vibration.

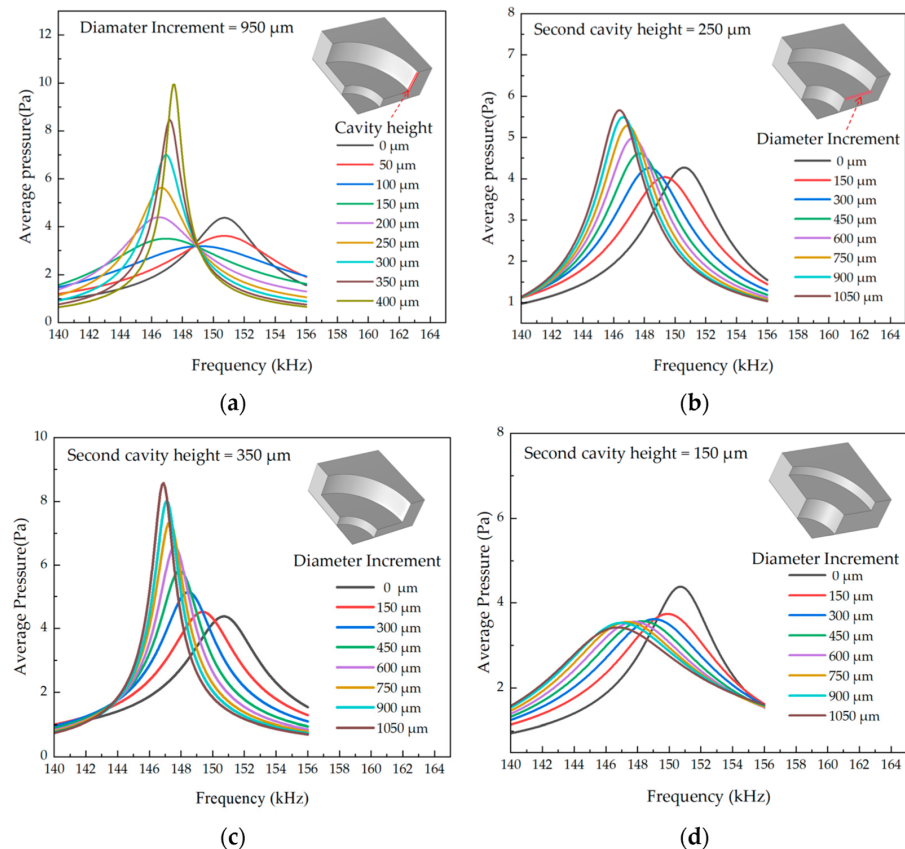


**Figure 3.** Average sound pressure results of FEM simulation at  $3\lambda$  below the PMUT resonance cavity: (a)  $D_i = 950\ \mu\text{m}$ , varying the height of the dilatation tube; (b)  $H_c = 250\ \mu\text{m}$ , varying the incremental

diameter of the dilatation tube; (c)  $H_c = 350 \mu\text{m}$ , varying the incremental diameter of the dilatation tube; (d)  $H_c = 150 \mu\text{m}$ , varying the incremental diameter of the dilatation tube.

Considering the process conditions and area limitations, the work in this paper produces PMUT cavity diameter increment  $D_i = 950 \mu\text{m}$  and expansion tube cavity height  $H_c = 250 \mu\text{m}$ , as well as FEM simulation geometry and far-field output average sound pressure, as shown in Figure 3a. The expansion tube PMUT below the  $3\lambda$  measured an average sound pressure gain of 27%,  $Q_{\text{tube-3db}} = 34$ ,  $Q_{\text{step-3db}} = 47$ . The FEM far-field SPL directivity normalization results are shown in Figure 4. The main lobe SPL sound field angle constriction and the side lobe level decreases, the stepped-tube PMUT side lobe compared to the primary lobe intensity decreased by 9 dB, while the tube PMUT side lobe is only reduced by 6 dB compared to the main lobe. The fabrication of the device for this paper will be presented in the third part.

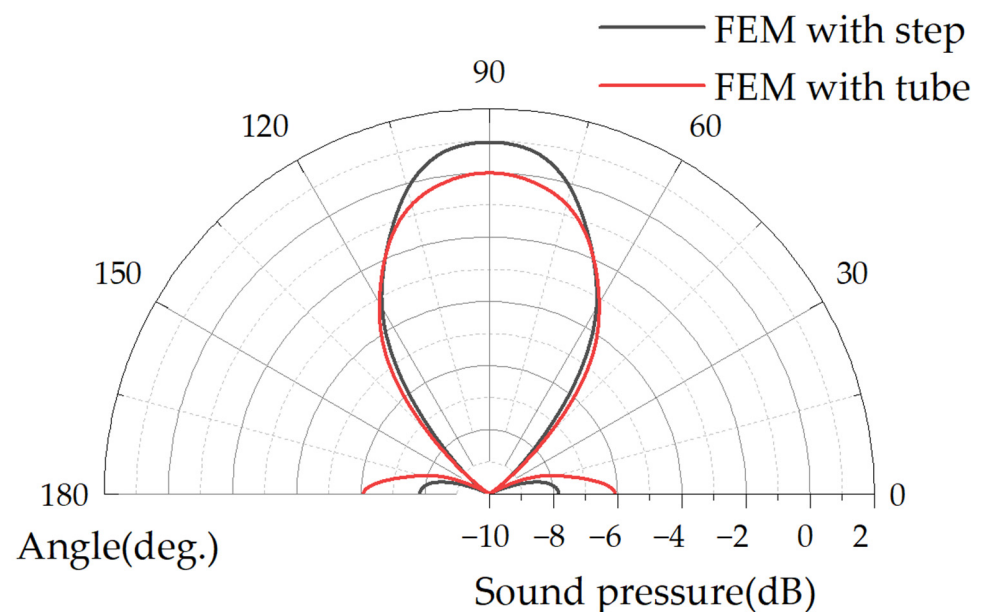


**Figure 4.** FEM simulated far-field SPL directivity normalized plot: red line is tube PMUT with 0 diameter increment at the end of the cavity; black line is stepped-tube PMUT with  $950 \mu\text{m}$  diameter increment at the end of the cavity and  $250 \mu\text{m}$  second backside cavity height.

### 3. Fabrication

As shown in the process flow in Figure 5, an eight-inch silicon-on-insulator (SOI) wafer, with a top silicon thickness of  $4 \mu\text{m}$  and a buried oxygen layer of  $500 \text{ nm}$ , is used for this work. First, a  $300 \text{ nm}$  layer of  $\text{SiO}_2$  is deposited on the surface with PECVD as a dielectric layer. Before the first deposition, the wafer needs to undergo pretreatment at a high temperature of  $450 \text{ }^\circ\text{C}$  for 5 min under vacuum. This process is designed to remove impurities and water vapor adhered to the SOI wafer [25]. Then, a one-step deposition of  $\text{Sc}_{0.096}\text{Al}_{0.904}\text{N}/\text{Mo}/\text{Sc}_{0.2}\text{Al}_{0.8}\text{N}/\text{Mo}$  stacked layers was carried out. The XRD and SEM results are shown in Figure 6. The full width at half-maximum (FWHM) value of  $1.58^\circ$  indicates that our deposited  $\text{Sc}_{0.2}\text{Al}_{0.8}\text{N}$  films have good crystalline quality, in which  $\text{Sc}_{0.096}\text{Al}_{0.904}\text{N}$  serves as the seed layer, which is favorable for the subsequent deposition of highly oriented films with the (002) orientation. This reduces the surface roughness of the  $\text{Sc}_{0.2}\text{Al}_{0.8}\text{N}$  film [16]. The resulting piezoelectric coefficients for the  $\text{Sc}_{0.2}\text{Al}_{0.8}\text{N}$  samples were  $d_{33} \sim 9 \text{ pm/V}$  and  $d_{31} \sim -4 \text{ pm/V}$  by the cantilever method. The seed layer, Mo electrode layer, and  $\text{Sc}_{0.2}\text{Al}_{0.8}\text{N}$  were all deposited using the Sigma<sup>®</sup> Standard PVD (Sigma<sup>®</sup> Deposition System from SPTS, Newport, UK). Pure Mo targets were used for the deposition under the Ar atmosphere, and an  $\text{Al}_{0.8}\text{Sc}_{0.2}$  alloy target was used for the deposition of the  $\text{Sc}_{0.2}\text{Al}_{0.8}\text{N}$  layer under the Ar/ $\text{N}_2$  atmosphere.

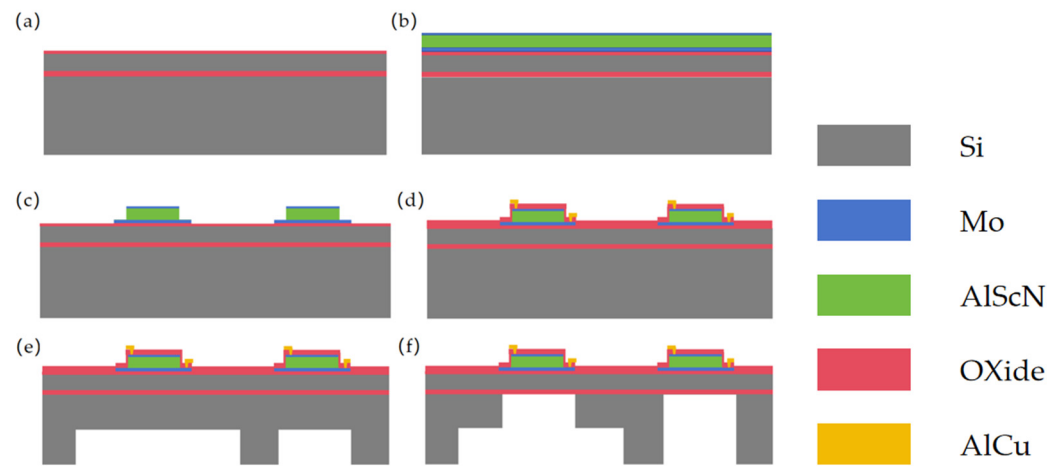


**Figure 5.** Process flow for fabrication of ultrasonic transducers with stepped-tube backside cavities based on  $\text{Sc}_{0.2}\text{Al}_{0.8}\text{N}$  films on eight-inch wafers: (a) starting from SOI wafers; (b) deposition of  $\text{Sc}_{0.096}\text{Al}_{0.904}\text{N}/\text{Mo}/\text{Sc}_{0.2}\text{Al}_{0.8}\text{N}/\text{Mo}$  stacks; (c) top Mo,  $\text{Sc}_{0.2}\text{Al}_{0.8}\text{N}$ , bottom Mo, dry etch patterning of the seed layer,  $\text{Sc}_{0.096}\text{Al}_{0.904}\text{N}$ ; (d) PECVD deposition, through-hole via etching, aluminum-copper alloy deposition and etching for PMUT metallization interconnections; (e) backside large cavity 250  $\mu\text{m}$  DRIE silicon etching; (f) backside tiny cavity silicon and  $\text{SiO}_2$  etching to release the membrane.

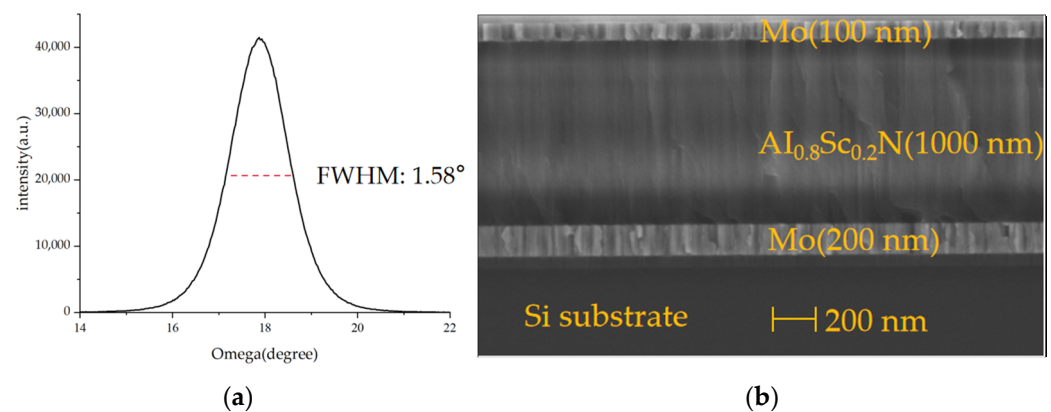


**Figure 6.** (a) XRD rocking curve measurement of  $\text{Sc}_{0.2}\text{Al}_{0.8}\text{N}$  (002) peak; (b) SEM scanning electron microscopy of  $\text{Mo}/\text{Sc}_{0.2}\text{Al}_{0.8}\text{N}/\text{Mo}$  film stack.

To optimize the etching slope angle and serve as a hard mask, a 400 nm layer of  $\text{SiO}_2$  was deposited by PECVD before  $\text{Sc}_{0.2}\text{Al}_{0.8}\text{N}$  etching, and the main etching process was carried out under a boron  $\text{BCl}_3/\text{Cl}_2/\text{Ar}$  atmosphere. In order to optimize the etching rate and improve etching homogeneity, we utilized the Inductively Coupled Plasma etching (ICP, Omega<sup>®</sup> etch system from SPTS, Newport, UK). Before the main etching process, we employed boron  $\text{BCl}_3/\text{Ar}$  gas for pretreatment. The native ScAlN oxide can be effectively removed by a short exposure to  $\text{BCl}_3/\text{Ar}$  plasma [26]. This is difficult to remove with the main etching gas on the film's surface, and it also increases the etching rate. It helps to reduce the problems of product yield caused by over-etching [27]. Then, a 200 nm  $\text{SiO}_2$  layer is deposited, and vias are etched to create interconnections between the bottom and top electrodes.

After metallized interconnects are etched, the wafer is flipped to the backside. Finally, the film is released using Deep Reactive Ion Etching (Rapier RP, Omega<sup>®</sup> etch system from SPTS, Newport, UK). In order to achieve a high depth-to-width ratio in deep silicon etching, the process dimensions of the PMUT stepped resonance cavity are achieved using the Bosch process to etch the bottom diameter of the stepped-tube backside cavity, which has a diameter of 1700  $\mu\text{m}$  [28]. The substrate height is controlled at 250  $\mu\text{m}$  through step-by-step etching. This is followed by PECVD deposition of a 400 nm  $\text{SiO}_2$  as a hard mask on the

backside of the wafer. The purpose of this deposition is to prevent the photoresist from melting due to the increase in wafer temperature caused by warpage. Warpage causes a gap between the wafer and the etch chamber platen, which can interfere with the second small resonance cavity etching process. The goal is to maintain optimal etching conditions. Finally, in order to improve the adhesion of the photoresist to the etched backside cavity, the backside was initially treated with HDMS (hexamethyl-disilazane), then coated with photoresist (C9005), and a secondary photolithography process was performed on the backside cavity with a diameter of 750  $\mu\text{m}$  using a double-sided aligned lithography machine (SUSS, MA/BA8 Gen3). Then, the 250  $\mu\text{m}$  SI was etched, and finally a 500 nm buried oxygen layer was etched to release the membrane.

## 4. Experiments

### 4.1. Electrical Characterization

An impedance analyzer measured the electrical parameters of the PMUT, and Figure 7 shows the electrical characteristics of a single PMUT, a tube backside cavity, and a stepped-tube backside cavity device, respectively.

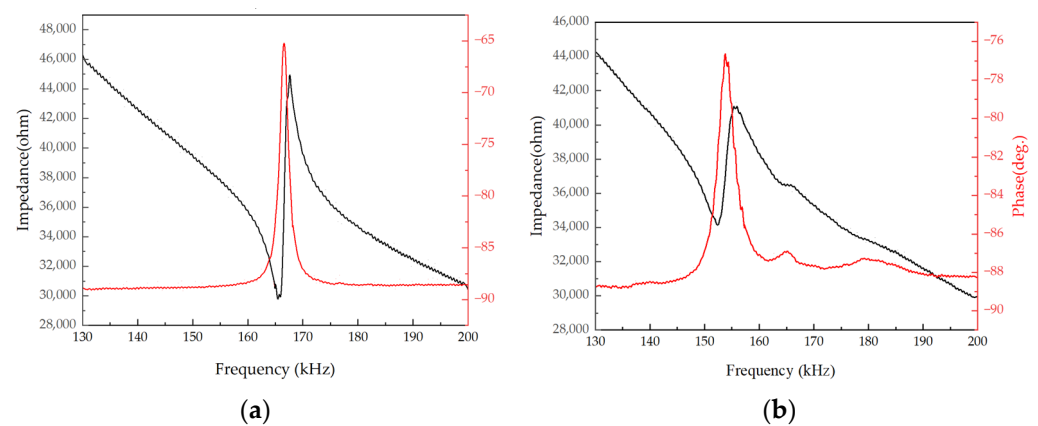


**Figure 7.** Device characteristics: (a) Tube PMUT electrical impedance characteristics; (b) Stepped-tube PMUT electrical impedance characteristics.

The discrepancy between the frequencies obtained from electrical tests and simulations can be attributed to the frequency shift caused by the stresses introduced during the deposition of the Mo/Sc<sub>0.2</sub>Al<sub>0.8</sub>N/Mo stacked films. The inclusion of the stepped resonance cavity alters the boundary conditions of the film in the vertical direction, resulting in a decrease in the stiffness of the structural layer. This leads to a reduction in the frequency of the PMUT in the stepped-tube backside cavity.

### 4.2. Acoustic Characteristics

The transmission performance of two PMUT structures was compared using the experimental setup shown in Figure 8. The experimental setup consisted of a rotating platform for PMUT, a function generator, a digital storage oscilloscope, a standard commercial microphone (CM16/CMPA, 2–200 kHz, Avisoft Bioacoustics Co., Ltd., Glienicke/Nordbahn, Germany), and a scale to measure shift distance. The PMUT was fixed onto the platform base, and the distance and angle between the sensor and the microphone could be adjusted by moving and rotating the bottom platform. During the experiment, the microphone was positioned 20 cm in front of the PMUT. The PMUT was driven by a function generator at its resonant frequency. The function generator produced 10 Vpp pulsed continuous square waves with a period of 10 cycles. The ultrasonic waves emitted by the PMUT propagated through the air and were received by the microphone. The received waves were then displayed on an oscilloscope. By rotating the circular bottom platform, the center axis of the PMUT and the microphone is set at 0°, 30°, and 60° when the acoustic time-domain characterization is shown in Figure 9. In the same experimental environment,

the acoustic energy at the front end of the PMUT in the stepped-tube backside cavity was more concentrated. The acoustic pressure was increased by 17% compared to that of the tube backside cavity. Compared to when the microphone and the PMUT were at  $0^\circ$ , the amplitude of the measured signal in the stepped-tube backside cavity were reduced by 75% and 81% when the PMUT was positioned at angles of  $30^\circ$  and  $60^\circ$ , respectively. In contrast, the amplitude signal of the tube backside cavity structure is only reduced by 11% and 32%.

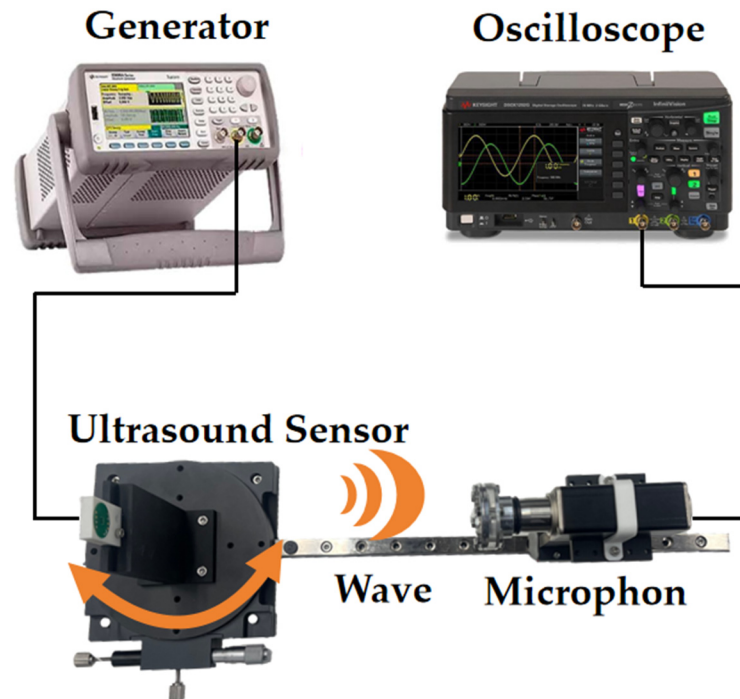


**Figure 8.** Schematic diagram of the angle experiment environment.

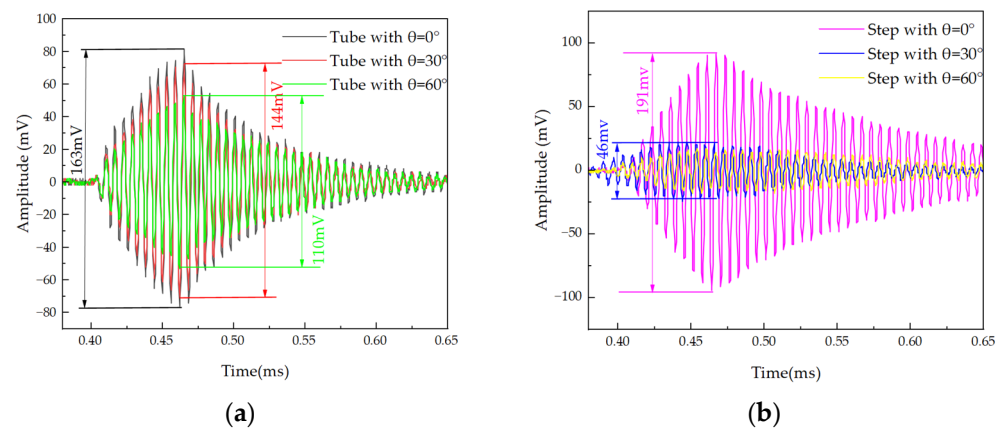


**Figure 9.** Device characterization for performance at different angles: (a) tube backside cavity PMUT transmitting characteristics; (b) stepped-tube backside cavity PMUT transmitting characteristics.

After receiving the excitation signal, the PMUT vibrates and emits ultrasonic waves accordingly. This vibration does not stop immediately, but rather it gradually becomes calm after the initial vibration with the help of the elastic layer. The period between the end of the initial vibration and the steady state is referred to as the ringing time [4]. The ringing time affects the range of the blind zone. Taking the transceiver as an example, the time difference between the input signal and the reflected wave is used to measure the distance of the detected object. When the ringing time is too long, it results in an overlap of the reflected signal and the ringing time, which affects the signal resolution [29]. The acoustic time-domain signals from the stepped-tube backside cavity and the tube backside cavity

PMUT are transformed by the FFT to obtain the  $BW_{\text{tube-3db}}$  of 5.16 kHz and the  $BW_{\text{step-3db}}$  of 3.34 kHz. The acoustic quality factor  $Q$  is calculated as 31 and 49, which is consistent with the simulation results. The structure of the backside cavity adjusts the impedance matching of the device. The stepped-tube backside cavity PMUT radiates more energy into the air at the same time. Therefore, acoustic measurements result in a higher quality factor  $Q$  compared to impedance measurements. But it will also bring adverse effects. For example, when it is used to measure distance, the echo signal from close objects will sometimes be obscured by the trailing signal.

Measurements were continued using the experimental conditions shown in Figure 8. These commercial microphones are relatively accurate across a range of frequency responses and do not require recalibration. The ultrasonic signal was measured every  $5^\circ$  rotation of the bottom platform in the same experimental environment. The results of the directivity of the device are shown in Figure 10. The half-power-beam-width ( $\theta_{-3\text{db}}$ ) of the tube backside cavity is approximately  $55^\circ$ , with two high secondary peak side lobes. These lobes reduce the sound pressure signal by 10% and 26%, respectively, compared to the main lobe. As a result, there is dispersion of acoustic energy and a decrease in the sound pressure of the PMUT in a single direction. The black curve represents the actual measurement of the stepped-tube resonant cavity, showing a half-power-beam-width ( $\theta_{-3\text{db}}$ ) of  $30^\circ$ . The introduction of the stepped-tube backside cavity reduces the half-power-beam-width ( $\theta_{-3\text{db}}$ ) of the PMUT by 45%. This reduction is achieved without significant generation of high secondary side lobes. Additionally, the sound pressure signal is reduced by 65% and 77%, respectively. Compared to that of the main lobe, the side lobe amplitude signal is reduced from 147 mV to 66 mV. When the PMUT is excited, the lack of isolation between the transducers leads to electrical, acoustic, and structural coupling. This coupling generates parasitic and spurious modes in the surrounding PMUT, which can interfere with the normal operation of the oscillator elements and even the entire PMUT array. This interference is known as crosstalk [30,31]. The stepped-tube PMUT has a smaller side lobe level, which theoretically reduces the array crosstalk effect caused by acoustic coupling in this study. The smaller acoustic field angle can help prevent echo interference in the non-detection direction during the ranging process.

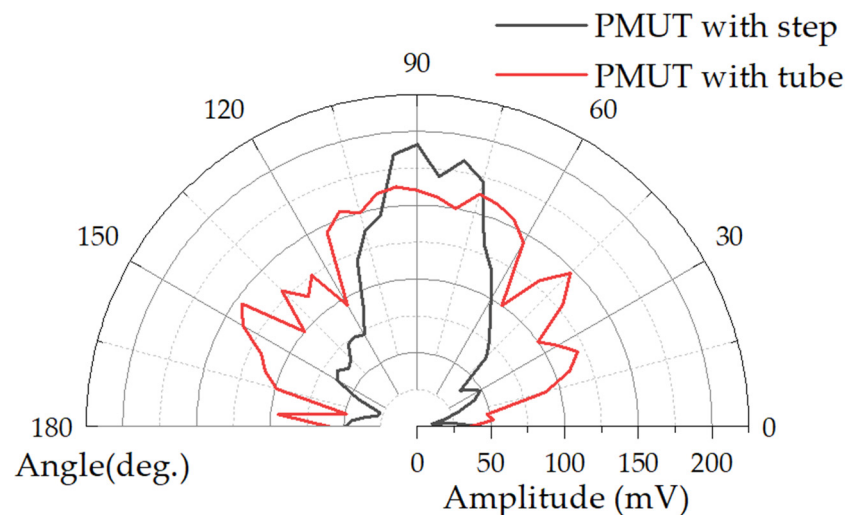


**Figure 10.** Measured far-field sound field angle of PMUT with tube and stepped-tube backside cavities.

## 5. Conclusions

In this paper, we demonstrate the performance of a stepped-tube PMUT based on a  $\text{Sc}_{0.2}\text{Al}_{0.8}\text{N}$  piezoelectric film. According to the FEM simulation results, reducing the side lobe level of the PMUT can be achieved by increasing the cavity height ( $H_c$ ) and the diameter increment ( $D_i$ ) of the second backside cavity layer. Taking advantage of the large back-cavity structure eliminates the need for a complex PCB package or a large external

horn. The effective radiating area is increased, resulting in improved acoustic output sound pressure. Acoustic experiments verified this conclusion, showing a 17% increase in average sound pressure at a distance of 20 cm, while reducing the half-power-beam-width ( $\theta_{-3\text{dB}}$ ) from 55° to 30°. The level of side lobe reduction for the emitted signal was 81%, while the reduction in the emitted signal from the tube resonant cavity PMUT was only 32%. The stepped-tube PMUT achieves a highly directional sound field and a lower side lobe level. The above experiments show that the stepped-tube backside cavity structure offers a new optimization approach for ScAlN MEMS PMUT devices, specifically for range proximity sensing and reducing array crosstalk effects.

**Author Contributions:** Conceptualization, supervision, writing—review, and editing, S.Z. and X.L.; Methodology, X.L., H.L. and A.S., data curation, writing—original draft preparation, validation, investigation, fabrication, X.L.; validation, investigation, project administration, funding acquisition, S.Z.; fabrication, X.L.; project administration, funding acquisition, S.Z. All authors have read and agreed to the published version of the manuscript.

**Funding:** This research was supported by the National Key Research and Development Program of China (No. 2021YFB3202500).

**Data Availability Statement:** The data are available within the article.

**Conflicts of Interest:** Authors Xiaobao Li, Haochen Lyu and Songsong Zhang were employed by the Shanghai Melon Technology Company Ltd. The authors declare that the research was conducted in the absence of any commercial or financial relationships that could be construed as a potential conflict of interest.

## References

1. Akasheh, F.; Myers, T.; Fraser, J.D.; Bose, S.; Bandyopadhyay, A. Development of piezoelectric micromachined ultrasonic transducers. *Sens. Actuators A Phys.* **2004**, *111*, 275–287. [[CrossRef](#)]
2. Tang, H.Y.; Lu, Y.; Jiang, X.; Ng, E.J.; Tsai, J.M.; Horsley, D.A.; Boser, B.E. 3-D ultrasonic fingerprint sensor-on-a-chip. *IEEE J. Solid-State Circuits* **2016**, *51*, 2522–2533. [[CrossRef](#)]
3. Przybyla, R.J.; Tang, H.Y.; Guedes, A.; Shelton, S.E.; Horsley, D.A.; Boser, B.E. 3D ultrasonic rangefinder on a chip. *IEEE J. Solid-State Circuits* **2014**, *50*, 320–334. [[CrossRef](#)]
4. Dausch, D.E.; Gilchrist, K.H.; Carlson, J.B.; Hall, S.D.; Castellucci, J.B.; Von Ramm, O.T. In vivo real-time 3-D intracardiac echo using PMUT arrays. *IEEE Trans. Ultrason. Ferroelectr. Freq. Control.* **2014**, *61*, 1754–1764. [[CrossRef](#)] [[PubMed](#)]
5. Xiu, X.; Yang, H.; Ji, M.; Lv, H.; Zhang, S. Development of mems airflow volumetric flow sensing system with single piezoelectric micromachined ultrasonic transducer (pmut) array. *Micromachines* **2022**, *13*, 1979. [[CrossRef](#)] [[PubMed](#)]
6. Przybyla, R.J.; Shelton, S.E.; Guedes, A.; Izyumin, I.I.; Kline, M.H.; Horsley, D.A.; Boser, B.E. In-air range finding with an ALN piezoelectric micromachined ultrasound transducer. *IEEE Sens. J.* **2011**, *11*, 2690–2697.
7. Wang, Y.; Zhang, L.; Wang, B.; Cai, J.; Gu, Y.A.; Lou, L.; Wang, X.; Wu, T. Microwave-induced thermoacoustic imaging with a multi-cell AlScN piezoelectric micromachined ultrasonic transducer. *Appl. Phys. Lett.* **2023**, *122*, 133702. [[CrossRef](#)]
8. Cai, J.; Wang, Y.; Jiang, D.; Gu, Y.; Lou, L.; Gao, F.; Wu, T. Photoacoustic Imaging Based on Broadened Bandwidth Aluminum Nitride Piezoelectric Micromachined Ultrasound Transducers. *IEEE Sens. Lett.* **2023**, *7*, 2500604. [[CrossRef](#)]
9. Sun, C.; Shi, Q.; Yazici, M.S.; Lee, C.; Liu, Y. Development of a Highly Sensitive Humidity Sensor Based on a Piezoelectric Micromachined Ultrasonic Transducer Array Functionalized with Graphene Oxide Thin Film. *Sensors* **2018**, *18*, 4352. [[CrossRef](#)]
10. Zhu, J.; Liu, X.; Shi, Q.; He, T.; Sun, Z.; Guo, X.; Liu, W.; Sulaiman, O.B.; Dong, B.; Lee, C. Development Trends and Perspectives of Future Sensors and MEMS/NEMS. *Micromachines* **2020**, *11*, 7. [[CrossRef](#)]
11. Liu, S.; Liao, J.; Huang, X.; Zhang, Z.; Wang, W.; Wang, X.; Yang, Z. Green Fabrication of Freestanding Piezoceramic Films for Energy Harvesting and Virus Detection. *Nano-Micro Lett.* **2023**, *15*, 131. [[CrossRef](#)] [[PubMed](#)]
12. Iqbal, A.; Mohd-Yasin, F. Reactive Sputtering of Aluminum Nitride (002) Thin Films for Piezoelectric Applications: A Review. *Sensors* **2018**, *18*, 1797. [[CrossRef](#)] [[PubMed](#)]
13. Ji, M.; Yang, H.; Zhou, Y.; Xiu, X.; Lv, H.; Zhang, S. Bimorph Dual-Electrode ScAlN PMUT with Two Terminal Connections. *Micromachines* **2022**, *13*, 2260. [[CrossRef](#)] [[PubMed](#)]
14. Nayak, B.; Gupta, H.; Roy, K.; Ashok, A.; Shastri, V.; Pratap, R. An Experimental Study of the Acoustic Field of a Single-Cell Piezoelectric Micromachined Ultrasound Transducer (PMUT). In Proceedings of the 2020 5th IEEE International Conference on Emerging Electronics (ICEE), New Delhi, India, 26–28 November 2020; pp. 1–4.
15. Yang, H.; Ji, M.; Xiu, X.; Lv, H.; Gu, A.; Zhang, S. AlScN Film Based Piezoelectric Micromechanical Ultrasonic Transducer for an Extended Long-Range Detection. *Micromachines* **2022**, *13*, 1942. [[CrossRef](#)] [[PubMed](#)]

16. Zhang, Y.; Miao, B.; Wang, G.; Zhou, H.; Zhang, S.; Hu, Y.; Wu, J.; Yu, X.; Li, J. ScAlN Film-Based Piezoelectric Micromechanical Ultrasonic Transducers with Dual-Ring Structure for Distance Sensing. *Micromachines* **2023**, *14*, 516. [[CrossRef](#)] [[PubMed](#)]
17. Rozen, O.; Block, S.T.; Shelton, S.E.; Horsley, D.A. Piezoelectric micromachined ultrasonic transducer with increased output pressure via concentric venting rings. In Proceedings of the 2015 Transducers—2015 18th International Conference on Solid-State Sensors, Actuators and Microsystems (TRANSDUCERS), Anchorage, AK, USA, 21–25 June 2015; pp. 670–673. [[CrossRef](#)]
18. David, T.B. *Fundamentals of Physical Acoustics*; Wiley: Hoboken, NJ, USA, 2000.
19. Senlik, M.N.; Olcum, S.; Koymen, H.; Atalar, A. Radiation impedance of an array of circular capacitive micromachined ultrasonic transducers. *IEEE Trans. Ultrason. Ferroelectr. Freq. Control.* **2010**, *57*, 969–976. [[CrossRef](#)] [[PubMed](#)]
20. Ju, X.; Gu, L.; Dong, X. Application and Research of Ultrasonic Horn in Ultrasonic Ranging System. *Sens. Transducers* **2014**, *170*, 60–66.
21. Bozkurt, A. A lumped-circuit model for the radiation impedance of a circular piston in a rigid baffle. *IEEE Trans. Ultrason. Ferroelectr. Freq. Control.* **2008**, *55*, 2046–2052. [[CrossRef](#)]
22. Wang, Q.; Lu, Y.; Mishin, S.; Oshmyansky, Y.; Horsley, D.A. Design, Fabrication, and Characterization of Scandium Aluminum Nitride-Based Piezoelectric Micromachined Ultrasonic Transducers. *J. Microelectromech. Syst.* **2017**, *26*, 1132–1139. [[CrossRef](#)]
23. Pierce, A.D. *Acoustics: An Introduction to Its Principles and Applications*; The ASA Press: London, UK, 2019.
24. Liu, X.; Zhang, Q.; Chen, M.; Liu, Y.; Zhu, J.; Yang, J.; Wang, F.; Tang, Y.; Zhao, X. Multiphysics Modeling and Analysis of Sc-Doped AlN Thin Film Based Piezoelectric Micromachined Ultrasonic Transducer by Finite Element Method. *Micromachines* **2023**, *14*, 1942. [[CrossRef](#)]
25. Zhang, Q.; Chen, M.; Liu, H.; Zhao, X.; Qin, X.; Wang, F.; Tang, Y.; Yeoh, K.H.; Chew, K.-H.; Sun, X. Deposition, Characterization, and Modeling of Scandium-Doped Aluminum Nitride Thin Film for Piezoelectric Devices. *Materials* **2021**, *14*, 6437. [[CrossRef](#)] [[PubMed](#)]
26. Xu, X.; Kuryatkov, V.; Borisov, B.; Pandikunta, M.; Nikishin, S.A.; Holtz, M. The effect of BCl<sub>3</sub> pretreatment on the etching of AlN in Cl<sub>2</sub>-based plasma. *MRS Online Proc. Libr.* **2008**, *1108*, 934. [[CrossRef](#)]
27. Yan, J.; Zhou, Y.; Zhang, S. Development of high uniformity Al<sub>1-x</sub>Sc<sub>x</sub>N piezoelectric film stack dry etching process on 8-inch silicon wafers. *Vacuum* **2023**, *210*, 111907. [[CrossRef](#)]
28. Lea, L.; Barker, L.; Hopkins, J. DRIE, an Enabling Technology for High Density Packaging. In Proceedings of the 2007 International Symposium on High Density Packaging and Microsystem Integration, Shanghai, China, 26–28 June 2007; pp. 1–3. [[CrossRef](#)]
29. Allan, J.Z. Acoustics: Sound Fields and Transducers. *J. Acoust. Soc. Am.* **2013**, *134*, 2337. [[CrossRef](#)]
30. Abdalla, O.M.O.; Massimino, G.; D’Argenzio, C.; Colosio, M.; Soldo, M.; Quaglia, F.; Corigliano, A. Numerical Simulation of Crosstalk Effects in PMUT Arrays. In Proceedings of the 2023 24th International Conference on Thermal, Mechanical and Multi-Physics Simulation and Experiments in Microelectronics and Microsystems (EuroSimE), Graz, Austria, 16–19 April 2023; pp. 1–5. [[CrossRef](#)]
31. Thao, P.N. Development of Linear pMUT Array with Low Mechanical Crosstalk Toward Ultrasonography Applications. In Proceedings of the 2021 21st International Conference on Solid-State Sensors, Actuators and Microsystems (Transducers), Orlando, FL, USA, 20–24 June 2021; pp. 659–662. [[CrossRef](#)]

**Disclaimer/Publisher’s Note:** The statements, opinions and data contained in all publications are solely those of the individual author(s) and contributor(s) and not of MDPI and/or the editor(s). MDPI and/or the editor(s) disclaim responsibility for any injury to people or property resulting from any ideas, methods, instructions or products referred to in the content.